J. Space Weather Space Clim. 2023, **13**, 2

https://doi.org/10.1051/swsc/2022039

JSWSC

Available online at:
www.swsc-journal.org

Topical Issue - Ionospheric plasma irregularities and their impact on radio systems

RESEARCH ARTICLE OPEN ACCESS

Characterization of local time dependence of equatorial spread F responses to substorms in the American sector

Shunzu Gao[1], Hongtao Cai[1,*], Weijia Zhan[3], Xin Wan[4], Chao Xiong[1,2], Hong Zhang[1], and Chen Xu[1]

[1] Department of Space Physics, Electronic Information School, Wuhan University, 430072 Wuhan, China
[2] Hubei Luojia Laboratory, 430079 Wuhan, China
[3] Space Weather Technology, Research and Education Center, University of Colorado Boulder, 80301 Boulder, USA
[4] Planetary Environmental and Astrobiological Research Laboratory (PEARL), School of Atmospheric Sciences, Sun Yatsen University, 519000 Zhuhai, China

Received 14 June 2022 / Accepted 1 December 2022

Abstract – Substorms have been found to play an important role in ionospheric electrodynamics at low and equatorial latitudes. In this study, we have investigated the possible influence of substorm on the generation of equatorial spread F (ESF). Coherent backscatter radar (JULIA) and incoherent scatter radar measurements between 2000 and 2017 at the Jicamarca Radio Observatory (11.95° S, 76.87° W, ~0° dip lat) are used. In statistical analysis, 12,525 h of ESF measurements are considered and have been divided into two groups based on their local time: post-sunset (18–24 LT) and post-midnight (00–06 LT). The superposed epoch analysis shows that the substorm-caused disturbance on vertical plasma drift can last longer than 12 h, which further affects the occurrence rate of ESF during a substorm. The increase/decrease of ESF at the post-sunset/post-midnight sector with about a 1 h lag to the substorm commencement is attributed to the prompt penetration electric field (PPEF), while the disturbance dynamo electric field needs approximately 3.5 h to suppress/promote the post-sunset/post-midnight ESF after substorm. In addition, the absolute value of correlation coefficients between the AE index and the occurrence rate of ESF is the largest when a 3–3.5 h lag is considered, which implies that the effect of disturbance dynamo electric fields could be more significant than prompt penetration electric field for the generation (suppression) of post-midnight (post-sunset) ESF during a substorm.

Keywords: Substorm / Equatorial spread F / Prompt penetration electric field / Disturbance dynamo electric field / Vertical plasma drift

1 Introduction

Equatorial spread F (ESF) is the name given to signatures of ionospheric F region electron density irregularities over a large range of scale sizes, which are observed using different types of measurements made at equatorial and low magnetic latitudes. During the past decades, the ESF has been investigated through a variety of space- and ground-based instruments (e.g. McClure & Hanson, 1977; Abdu et al., 1981; Burke et al., 2009; Wan et al., 2018). As ESF can seriously disturb the communication and navigation systems and interfere with surveillance operations (Doherty et al., 2004; Sunda et al., 2015), it is crucial to comprehend the ionosphere-thermosphere interactions that lead to the generation of ESF (Conker et al., 2003; Hlubek et al., 2014; Xiong et al., 2016b). The generation of ESF is commonly explained by the Generalized Rayleigh–Taylor instability (RTI, Sultan, 1996; Basu, 2002). The absence of sunlight after sunset in the E region and much faster recombination at lower altitudes than at higher altitudes combine to create a steep vertical plasma density gradient in the bottom side F region, which is opposite to the direction of the gravitational force (e.g. Kelley et al., 1981; Singh et al., 1997). This configuration is unstable. A disturbance at the bottom side F-region can develop and be lifted up into higher altitudes via the enhanced E × B during pre-reversal enhancement (PRE, Kelley et al, 1976; Fejer, 2011), and finally form the well-developed plasma irregularities at the topside ionosphere that are elongated along the magnetic flux tubes (Fejer et al., 1999).

The occurrence of ESF depends on various factors, such as longitude, latitude, local time, seasons, and solar activity (Aarons, 1993; Fejer et al., 1999; Hysell & Burcham, 2002; Xiong et al., 2010; Watanabe & Oya, 2010; Paul et al., 2018; Singh & Sripathi, 2020). It is also found that the ESF occurrence at magnetically disturbed periods differs from their quiet time pattern

*Corresponding author: htcai@whu.edu.cn

(Abdu et al., 2003; Kikuchi et al., 2008; Wan et al., 2019; Zhang et al., 2021a). During geomagnetic storms, the low latitude and equatorial ionosphere are affected by two sources: (1) the enhanced dawn-dusk electric fields at high latitudes under southward interplanetary magnetic field (IMF) conditions can penetrate almost instantaneously to the low latitude and equatorial region, known as the prompt penetration electric field (PPEF) (e.g. Kikuchi et al., 2000; Hui et al., 2017; Simpson & Bahr, 2020), and (2) the energy input into the thermosphere at high latitudes produce equatorward winds, which turn westward at middle and low latitudes due to the Coriolis force (e.g. Xiong et al., 2015, 2016a; Zhang et al., 2021b). The disturbance wind will generate a westward/eastward electric field on the dayside/nightside at low latitudes, which opposes their quiet-time patterns, known as disturbance dynamo electric field (DDEF) (e.g. Blanc & Richmond, 1980; Xiong et al., 2015). The equatorial ionospheric perturbations during disturbed conditions are affected by the combined effects of PPEF and DDEF from the high-latitude ionosphere. Hence the effect of geomagnetic storms in the context of generation/inhibition of ESF is an important space weather concern and has received a lot of attention in the recent past (Li et al., 2018; Cherniak & Zakharenkova, 2022; Zhang et al., 2022). Li et al. (2018) showed that strong southward IMF Bz excursions during storms rapidly raised the F layer near sunset and led to the development of intense equatorial plasma irregularities. Aa et al. (2019) presented post-sunset intense plasma bubble observations over China and adjacent areas and suggested that the high-altitude plasma depletions were driven by strong equatorial prompt penetration electric fields.

Apart from geomagnetic storms, substorms also cause disturbance in the electric field at the low-latitude ionosphere, which contributes to the generation and development of ESF. By analyzing two abnormal vertical plasma drift events observed by Jicamarca Unattended Long-term Investigations of the Ionosphere and Atmosphere (JULIA) radar, Hui et al. (2017) showed that substorms can induce both eastward and westward penetration electric fields under steady southward interplanetary magnetic field (IMF Bz) conditions. Using vertical drift observations from Jicamarca and magnetic field observations of the equatorial electrojet over the Philippines, Rout et al. (2019) analyzed the large electric field disturbances in the equatorial ionosphere during the September 2017 geomagnetic storm. They pointed out the significant contribution from substorm to electric field disturbances. Fejer et al. (2021) used Jicamarca radar measurements to study the response of equatorial ionospheric electrodynamics and spread F during the main phase of this geomagnetic storm. They suggested that the occurrence of storm-time substorms is one of the major factors causing the large nighttime westward and eastward electric field perturbations. They also concluded that substorm electric fields play significantly more important roles in the electrodynamics of the equatorial ionosphere than has been previously acknowledged. These investigations reveal that storm-time substorm electric fields have an important effect on the electrodynamic processes of the low-latitude ionosphere, but it is not clear how non-storm-time substorms affect ionospheric irregularities in different local time sectors. In addition, although the intensities of substorms are weaker compared with magnetic storms, they occur more frequently and therefore have also a significant influence on the magnetosphere and ionosphere (Kamide et al., 1998).

This study intends to better understand the impact of non-storm time substorms on the generation of ESF. In this study, we took advantage of the long-term observations of equatorial F region irregularities made by the 50 MHz coherent backscatter radar (JULIA) of the Jicamarca Radio Observatory (Hysell & Burcham, 2002). In particular, we divided the ESF observations at substorms into two local time sectors, due to the local time dependence of the disturbed electric field. To better reveal the relation between substorm and ESF, the vertical plasma drift data from the incoherent scattering radar (ISR) at Jicamarca was employed. In the following sections, we first briefly describe our measurement techniques, data analysis approach, and the selected data in Section 2. Then we present the results in Section 3 and the discussion in Section 4. Section 5 provides a summary of our findings and key conclusions.

2 Methodology

2.1 JULIA and Jicamarca ISR

The JULIA radar is a 50 MHz coherent backscatter radar system that is part of a set of ground-based instruments located at the Jicamarca Radio Observatory (Hysell & Burcham, 2002). In the initial implementation of JULIA, two 30 kW transmitters were utilized to excite the North and South quarters of the Jicamarca antenna (Zhan et al., 2018). These transmitters were coupled to maximize the directivity of the combined pattern in the direction perpendicular to the geomagnetic field at F-region heights. This increases the sensitivity of the system to field-aligned irregularities. Receivers were connected to the east and west quarters of the antenna, which afforded a zonal interferometry baseline approximately 34 wavelengths long. This configuration enabled interferometric analysis of the echoes and the determination of the zonal component of irregularity velocity. Since 1996, Modifications of JULIA have been made so that the system continued to be able to make routine (150–200 days per year) coherent backscatter radar observations of daytime and nighttime echoes caused by field-aligned ionospheric irregularities at E- and F-region heights. The measurements used in this study consist of the signal-to-noise ratio (SNR) of the nighttime F-region echoes observed by JULIA from 2000 to 2017. For nighttime F-region observations, the measurements typically start at 1800 LT and end at around 0800 LT the next day. The measurements made by JULIA cover altitudes ranging from about 90 km to 800 km or above (Zhan et al., 2018).

The vertical plasma drifts used in this study were derived from Jicamarca Radio Observatory incoherent scatter radar data between 2000 and 2017. The measurements cover different geophysical conditions over approximately two solar cycles. Careful inspection of the data files shows that measurements for 531 different days are available. It is important to note that the amounts of measurements vary from day to day. While some days have a full 24 h of measurements, other days have only a few hours of observations available. Jicamarca is the only magnetic equatorial site that can accurately measure vertical and zonal drifts as a function of time and height. The drifts were

measured typically at altitudes from about 250 to 800 km with a height resolution of 20–45 km and with an integration time of 5 min. The values used in this study represent 15-minute averages at altitudes from about 250 to 600 km, where the signal-to-noise ratios are highest (Navarro et al., 2019).

2.2 Data selection

Our investigation focuses on the effect of substorms on the F region plasma irregularities, so the effect of geomagnetic storms should be excluded as much as possible. Although substorms often occur during magnetic storms, they are not always accompanied by magnetic storms or low SYM-H (Kamide et al., 1998). To exclude storm time observations, we first identified the onset of geomagnetic storms using the SYM-H index. The Dst index or SYM-H index is widely used to define disturbed magnetic storms. The most often-used definition of a geomagnetic storm is an event wherein the minimum of the Dst index goes below a critical value, for example, −50 nT or −100 nT (Borovsky & Shprits, 2017). Here, the moment when the SYM-H index dropped to −50 nT was defined as the onset time of the storm's main phase. Based on the above method, 513 storm events were determined during 2000–2017. Numerous studies have demonstrated that the influence of storms on the ionosphere can last from hours to days, but significant impact mainly occurred within approximately 24 h. Hence, to eliminate the effect of a magnetic storm as much as possible, the data between −12 and 36 h from magnetic storm onset time was removed. It is possible that the impact of a few events still exists, but it will not have a significant impact on the statistical results. Our selection criteria resulted from the best compromise between data quality and availability. To examine the statistical response of ESF to substorms, we analyzed JULIA observations collected between 2000 and 2017. The available observations for this investigation included an extensive variety of solar flux conditions. The change in solar flux is approximated by the P107 index, which reflects the intensity of EUV radiation. P107 is calculated by F107 and as:

$$\mathrm{P107} = \frac{1}{2}\left(\mathrm{F107} + \overline{\mathrm{F107}_{81\,\mathrm{days}}}\right), \tag{1}$$

where $\overline{\mathrm{F107}_{81\,\mathrm{days}}}$ represents the 81-day average of the F107 index. Numerous studies have demonstrated that P107 is a more linear indication of the ionospheric response to solar EUV irradiation than F107, which emphasizes the shorter activity periods (e.g. Rentz & Lühr, 2008). The variation of the P107 and AE index over the observation period (2000–2017) is shown in the top panel of Figure 1a. It covers two solar maximums and two minimums including the extreme solar minimum of 2008–2009. The database encompasses a wide span of solar fluxes ranging from 70 to 250 solar flux units (SFU, 1 SFU = 10^{-} W · m^{-} · Hz^{-1}). The data is categorized into three solar activity segments: low solar activity years (P107 < 90), moderate activity years (P107 in [90, 120]), and high solar activity (P107 > 120). Besides, the observation time of JULIA for each day is presented in the bottom panel of Figure 1a. The observations are comprehensively distributed over years, and the time is about 5 h on most days.

In this study, geomagnetic substorms activities were characterized by auroral electrojet (AE) and the upper component of auroral electrojet index (AL). An AL-based identification of substorm onsets algorithm was adopted, which was proposed by Newell and Gjerloev (2011). The specific substorm determination process is as follows. An onset was identified at t_0 when four conditions are satisfied:

$$\mathrm{AL}(t_0+1) - \mathrm{AL}(t_0) < -15\,\mathrm{nT}, \tag{2}$$

$$\mathrm{AL}(t_0+2) - \mathrm{AL}(t_0) < -30\,\mathrm{nT}, \tag{3}$$

$$\mathrm{AL}(t_0+3) - \mathrm{AL}(t_0) < -45\,\mathrm{nT}, \tag{4}$$

$$\sum_{t=4}^{30} \mathrm{AL}(t_0+i)/26 - \mathrm{AL}(t_0) < -100\,\mathrm{nT}. \tag{5}$$

Further, recurrent substorms which were preceded by another onset over the previous 2 h were excluded. Based on the identification algorithm, 10,416 sole substorms (excluding the reoccurrence of substorms) events were detected during 2000–2017. Figure 1b shows the local time distribution of substorm events. These events were almost evenly distributed in each local time. The number was slightly higher with nearly 500 events at each hour during 02–06 and 16–18 LT, but during other local times, 350–450 events were observed in each hour. The number of substorm events from dusk to midnight is slightly less than that from midnight to dawn, but still at the same level. The AE/AL and related indexes are 5-minute averages obtained from the NASA Omni database (https://cdaweb.gsfc.nasa.g-ov/index.html). Geomagnetic substorm activities were characterized by the auroral electrojet (AE) index. To investigate the time evolution of the average AE index after substorm, Figure 1c displays the superposed epoch analysis of the average AE from epoch time $\Delta t = -3$ to 30 h for each local time. At the key time, $\Delta t = 0$ h, an increase in the AE index can be found for all the local times. Then it decreased gradually with epoch time, showing a single peak feature. During nighttime (1800–0600 LT), AE is generally below 180 nT after $\Delta t = 12$ h. Therefore, in the following analysis, we will mainly focus on −3 to 12 h and ignore the effects of continuous substorms.

2.3 Irregularity identification

The ESF was identified based on the number of echoes above a certain SNR within a time versus height interval. Height variation of ESF is not considered in this study. The observations for each day were grouped in time series with an interval of 15 min. There are 33718 15-min intervals (bins) in total. The echo number was counted and only 5% of bins have echoes within 0 and 50. The median number is 450, and the mean number is 804, which was enough for statistics. When 30 or more coherent echoes with SNR greater than −20 dB were observed in each time interval, it was characterized as an ESF epoch, otherwise, it was characterized as a non-ESF epoch (Zhan & Rodrigues, 2018). The SNR threshold (−20 dB) and the number of echoes (at least 30) were chosen to minimize the misidentification of interference and clutter as echoes caused by ESF. In this study, data were divided into 6 data sets according to local time and the 10.7 cm solar flux index. The occurrence rate of ESF was obtained as a function of superposed epoch time for each dataset. The epoch time is binned into intervals of

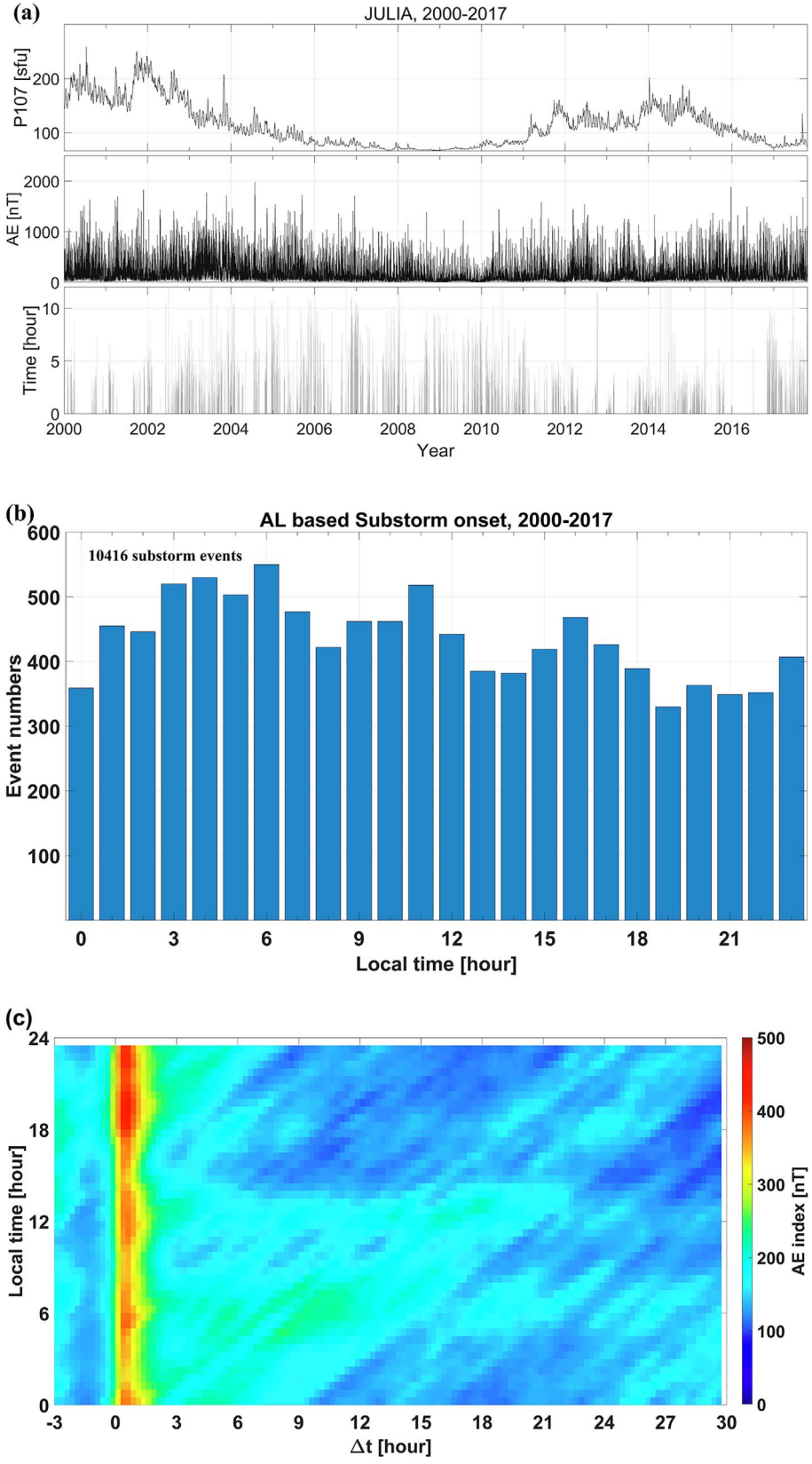

Figure 1. (a) Variation of the solar flux index (F10.7) and AE index during the period under which JULIA measurements were made. (b) Local time distribution of substorm events. (c) The average temporal evolution of the AE after a substorm at the key time (Δt = 0).

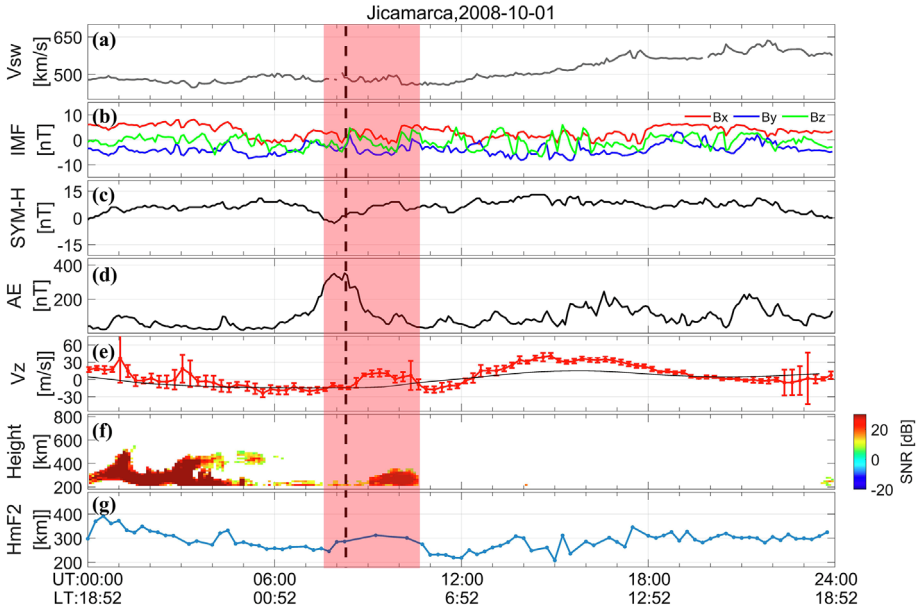

Figure 2. (a) Solar wind velocity, Vsw. (b) Interplanetary magnetic field, IMF. (c) SYM-H index. (d) AE index during October 1, 2008. (e) Average vertical drifts (red line) over Jicamarca. Error bars denote the standard deviations on the average drifts. The black curve shows the corresponding quiet time patterns. (f) An example of the Range-Time-Intensity map of echoes measured by JULIA. (g) Average HmF2 over Jicamarca on October 1, 2008.

15 min. The occurrence rate for each epoch time interval was calculated by taking the ratio between the number of ESF epochs and the total number of epochs included in the interval.

3 Results

3.1 Post-midnight ESF event during substorm

In this section, we first presented a typical post-midnight ESF event on October 1, 2008, when an independent substorm occurred. Figure 2 summarizes the important observations in this case, with the time periods of substorm and ESF events shaded in red rectangles. The time when the south IMF Bz turns north is indicated by the black vertical dotted line. The P107 index for the day is 67.0, which is at a low activity level.

The top four panels (a–d) of Figure 2 depict the variations of the geophysical parameters during this event. Universal time (UT) and the corresponding local time (LT) at Jicamarca is shown at the bottom of Figure 2. Solar wind and interplanetary magnetic field parameters are 5-minute averages obtained from the NASA OMNI database. Figure 2a shows solar wind radial velocity (V_{sw}), followed by the X, Y, and Z components of IMF, SYM-H, and AE index. Throughout this period, the solar wind radial velocity changes slowly without any drastic increase until 15:00 UT (about 09:52 LT). The IMF Bz fluctuated slightly and occasionally changed polarity with its value varying from −5 nT to 5 nT with a north turning occurring at about 08:20 UT (local time 02:10 LT). The SYM-H fluctuated steadily and remained above −15 nT during this period, indicating that there is no magnetic storm activity. The AE index on the other hand remained less than 100 nT until 07:00 UT (01:52 LT) when it started to increase rapidly beyond 300 nT at around 07:30 UT (02:40 LT), which is a sign of substorm commencement in our study and is recorded as the key moment.

The three bottom panels (e–g) of Figure 2 summarize the radar observations over the Jicamarca site before and after the substorm on October 1, 2008. Plasma drifts and spread F irregularities were measured from 200 to 800 km with a 15-km range resolution and a 5-min integration time. Figure 2e shows the vertical plasma drift measurements. Drift measurements at altitudes below 200 km were often less accurate, and they were not included in our averages. The error bars in the panel represent the standard deviations on the average drifts, which are always larger than the measurement errors. The black line in this panel shows the quiet time vertical drift pattern. The increase of upward drifts during around 00:00–04:00 UT (18:52–22:52 LT) before the substorm corresponds to the pre-reversal enhancement (PRE), then it returns to quiet time level until 08:20 UT (03:12 LT). The vertical drift quickly increases at about 45 min after the key moment of substorm at 08:20 UT and reaches around 20 m/s, which departs from the quiet time downward drift pattern (black line). It is clearly seen that the increase of vertical drift occurred almost simultaneously with the north turning of IMF Bz. This could be deduced by overshielding electric fields. Numerous existing studies have confirmed that the overshielding electric field during a substorm is strong enough to cause electric field disturbance in the equatorial ionosphere (e.g. Huang, 2009; Huang, 2012; Hashimoto et al., 2017), matching the dusk-to-dawn electric field associated with the R2 FACs. Huang (2012) found that substorm induces an eastward electric field in the dayside equatorial ionosphere. Hashimoto et al. (2017) showed that overshielding often occurs during the substorm recovery due to the convection reduction, resulting in a dusk-to-dawn electric field at low latitudes on the nightside. Hence, we attribute the disturbance vertical drift

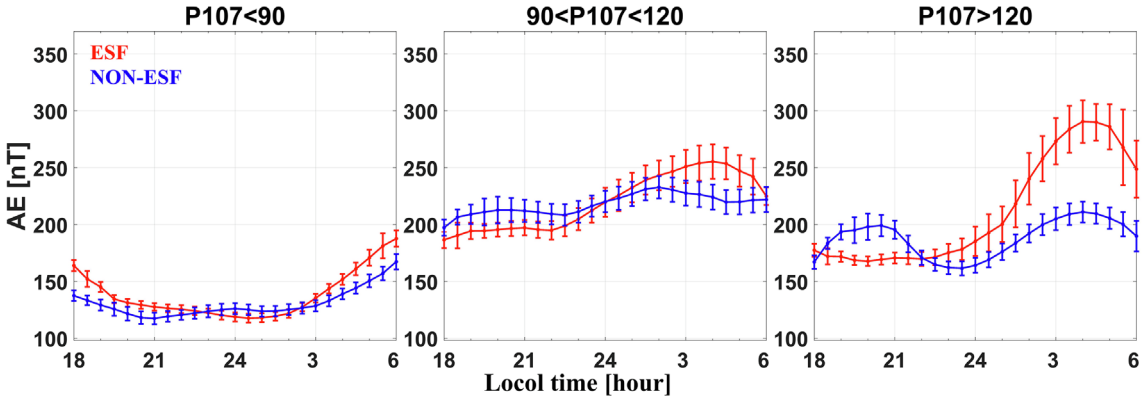

Figure 3. The AE index as a function of local time under with/without ESF conditions.

in this event to the overshielding electric field. It should be noted that the variations of IMF Bz are not associated with substorms, particularly the onset time of substorms and Bz turnings are separated by sufficiently large time, but the orientation of IMF Bz can be used as evidence for the overshielding electric field.

Figure 2f illustrates the Range-Time-Intensity (RTI) map of the coherent backscatter power from equatorial spread F irregularities measured by the west beam. The RTI map shows significant post-sunset ESF during 18:52–23:15 LT, and it also indicates a post-midnight ESF event that started around 03:50 LT. The echoes indicate a bottom-type ESF at 200–300 km. Figure 2g exhibits the virtual height of the base of the F2 layer (hmF2) estimated from collocated digisonde observations. HmF2 was at its lowest around 01:00 LT and began to rise around 02:30 LT, when the drift was about to turn upward from −10 m/s, supporting Nicolls et al. (2006)'s hypothesis of apparent uplifts associated with upward perturbation drifts. It should be noted that the drift result clearly shows that the post-midnight increase in this event is independent of the PRE. Meanwhile, this layer uplift corresponded to the increase of vertical drift velocity and was followed by the ESF. It can be inferred that the post-midnight ESF is more associated with ionospheric conditions after midnight, not a continuation of the post-sunset ESF. The observation results show that during the substorm, a post-midnight ESF is generated in the American sector due to the substorm overshielding the electric field.

3.2 Statistical results

To explore the specific role of substorms on the occurrence of ESF, the variation of the average AE index as a function of local time is provided for ESF and non-ESF epochs, as shown in Figure 3. Error bars denote the standard deviations on the average AE index. It can be seen that the AE index exhibits different trends under conditions with or without ESF. During low solar flux periods (LSF), the AE index under ESF conditions declines sharply from 18–20 LT and remains at a low level from 20:00–03:00 LT with a mean value of about 130 nT. It rises at about 03 LT. While the AE index under ESF conditions remains stable, and the average value is about 145 nT. During middle solar flux (MSF), the AE index increases slowly with LT for both ESF and NON-ESF conditions. What is different is that from 18–03 LT, the AE index with ESF is smaller. After 03 LT, it becomes higher the than AE index with ESF. This discrepancy is more significant during high solar flux (HSF) conditions. The AE index with ESF increases to 300 nT at 06 LT, when the AE under non-ESF conditions remains around 190 nT. The result shows different characteristics of local time variation of AE under with and without ESF conditions, indicating that the AE index plays different roles in the development of ESF for different local time sectors. Therefore, we infer that the enhancement of geomagnetic activity associated with substorms has effects on the equatorial ionospheric irregularities in the American sector.

In order to assess the response of ESF and plasma drift to substorms, we performed a superposed epoch analysis of the occurrence rate and vertical drifts. The perturbation values of the occurrence rate and vertical drifts are determined by subtracting the average value during the quiet period. Results for epoch times ranging from −3 to 12 h are provided to concentrate on the main effect of a single substorm. In addition, several researchers have reported different occurrence rates in the pre-midnight and post-midnight sectors (e.g. Li et al., 2011; Wan et al., 2019). The high occurrence rate of ESF events observed in the post-sunset sector is due to the PRE, while the post-midnight sector is not expected to be favourable for the development of the ESF in most cases (Zhan et al., 2018). A high occurrence rate of the F region echoes during post-midnight hours is observed only under June solstice and low solar flux conditions (Thampi et al., 2009; Huang & Hairston, 2015; Smith et al., 2016). Figure 3 also indicated the different roles of the AE index in the generation of ESF before and after midnight. Hence, in this study, the coherent backscatter radar measurements were sorted into two LT bins: post-sunset (18–24 LT) and post-midnight (00–06 LT). The temporal evolution for different local time sectors is shown with different colours. Also, the results are presented for three solar flux conditions.

To better visualize the storm effects on the ESF occurrence, we calculated the residual value regards to the ESF occurrence under magnetic quiet periods. The residual occurrence is plotted in Figure 4a and labelled as residual occurrence. For two local time sectors, the residual occurrence varies around zero, but in different ways. During low solar flux conditions, the residual occurrence rate of post-sunset ESF decreases from −3 h to −1 h and is then followed by an increase at $\Delta t = -1$ h. The maximum value of 5% is observed at $\Delta t = 1.5$ h, indicating a significant promotion by substorms. Then from $\Delta t = 1.5$ to

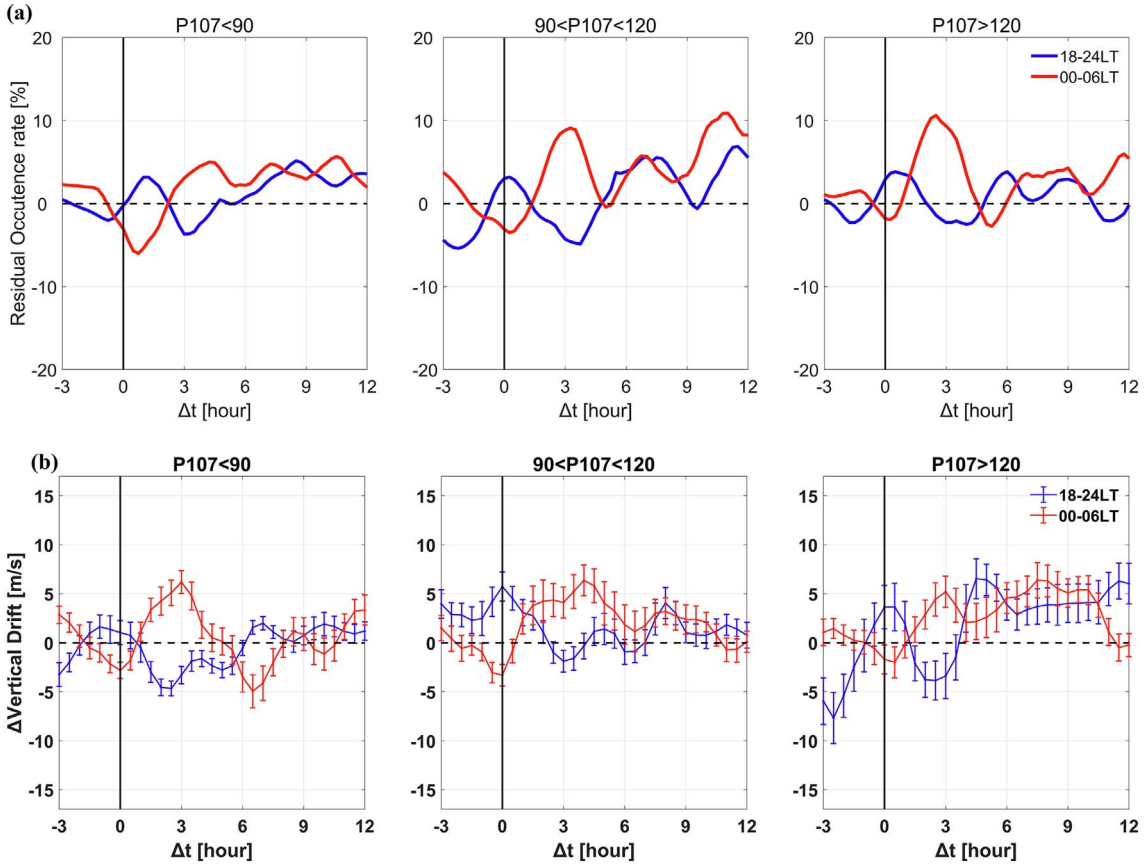

Figure 4. The superposed epoch analysis of disturbance after a substorm at the key time (Δt = 0) for: (a) residual value to quiet-time level of ESF occurrence rate, (b) disturbance vertical plasma drift.

3 h, the residual occurrence rate of post-sunset ESF decreases to its minimum value, which is about −4%. While for post-midnight ESF, the residual occurrence rate exhibits the opposite tendency to that observed in the post-sunset sector. It decreases from Δt = −1.5 h and reaches the minimum value of −6%. Thereafter, it gradually rises, reaching a maximum of 6% at approximately Δt = 4.5 h. The presence of residual occurrence rate indicates that substorms have opposing effects on the ESF in two local time sectors. Under moderate and high solar flux conditions, similar variation is observed. The performance of the residual occurrence rate is consistent with that of low solar activity, but the fluctuation magnitude is distinct. Figure 4a shows that substorms have a significant impact on the occurrence of ESF. Both enhancement and reduction relative to quiet-times level are observed, depending on the local time as well as the epoch time Δt.

To better understand the response of residual occurrence rate, we checked the response of perturbation vertical drift to substorms using the superposed epoch analysis. The result was presented in Figure 4b. In the same way as the residual occurrence rate, drifts were sorted into the two local time bins. Concerning the uncertainty of the derived variations, we obtain typical values for standard deviation (σ) of about 10 m/s for the disturbance drifts at each epoch time Δt. More important for our analysis is the uncertainty of the mean value. It is defined as $\sigma/\sqrt{n}$, where n is the number of events contributing to each Δt point. Figure 4b shows a more prominent response during post-midnight (00–06 LT). Therefore, we are more interested in this local time sector. From Figure 4b, it can be seen that during low solar flux, the post-midnight perturbation drift starts to decrease from Δt =−3 h to 0 h, reaching a value of −3 m/s. Then it goes up and reaches its peak of 6.7 m/s at around Δt = 2.5 h. While for the 1800–2400 LT sector, the disturbance drift shows the opposite pattern. The perturbation drift starts to increase at Δt = −3 h. It reaches the peak value of −3 m/s at Δt = 0 h, followed by a decrease from 0 to around Δt = 3 h when the minimum value of −5 m/s. A remarkable feature is that the disturbance drift is consistent with the change of ESF, which helps to better understand the response mode of ESF occurrence rate. It can be concluded that perturbation drifts play a crucial role in the variation of ESF occurrence rate. In addition, the variations of perturbation drift during middle solar flux and high solar flux are similar to that of low solar flux at both local time sectors, indicating that the electric field perturbations during substorms do not vary with the solar flux condition.

4 Discussion

We have investigated the response of the ESF occurrence rates at Jicamarca to substorm events according to an AL-based identification algorithm proposed by Newell and Gjerloev (2011). The local dependence of ESF concurrence rate is closely related to the disturbed vertical plasma drifts (zonal electric

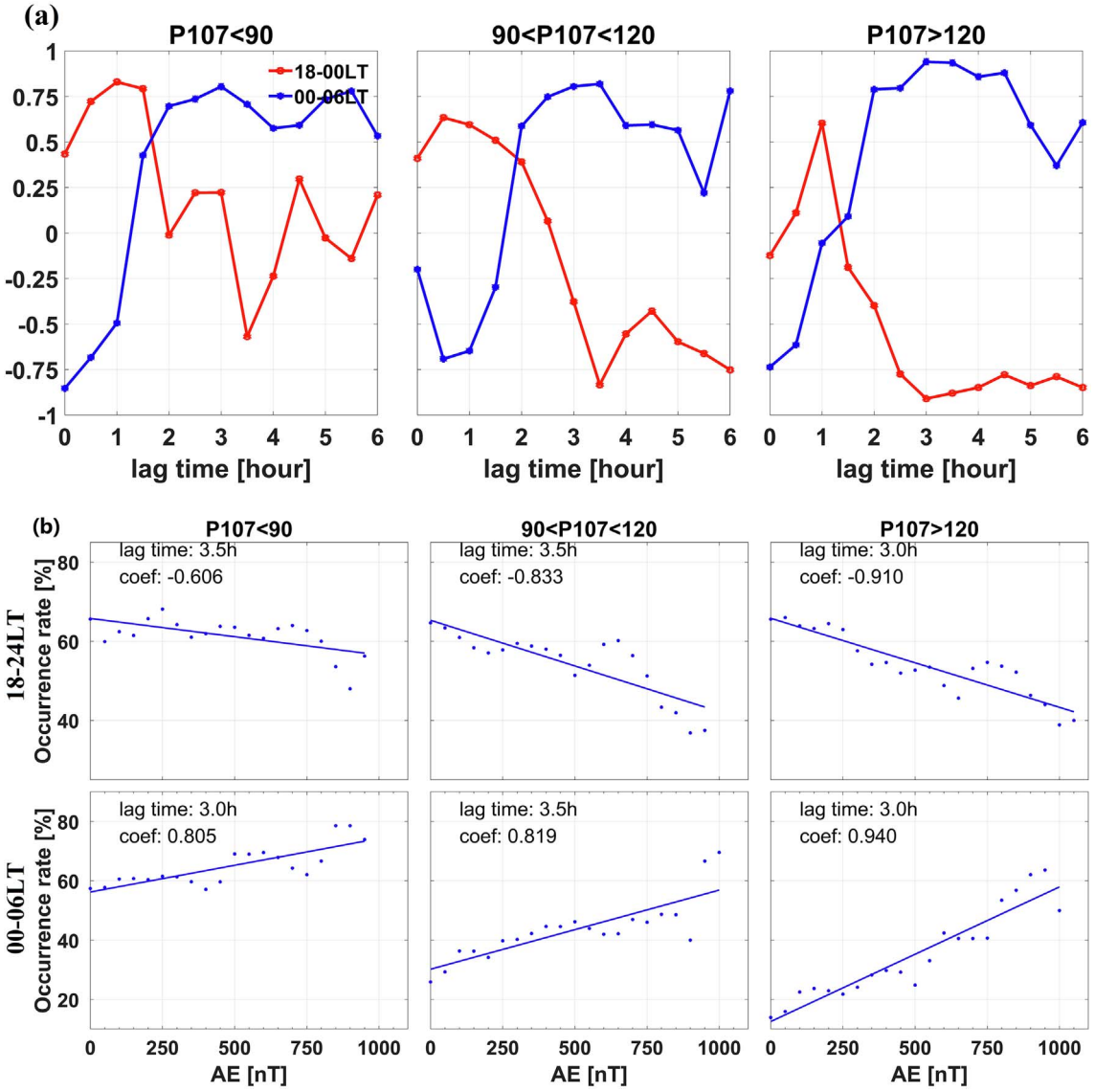

Figure 5. (a) The correlation coefficients between the ESF occurrence rate and the AE index from 0 to 6.0 h of delay time. (b) The ESF occurrence rate in relation to AE index for different solar flux conditions, the top and bottom panels correspond to the post-sunset and post-midnight, respectively.

fields). In this section, we will further discuss the functions of PPEF and DDEF in the generation of ESF in different local time sectors, and investigate the implications of the local time dependence.

4.1 Effect of PPEF and DDEF

Our superposed epoch analysis results revealed that the fluctuation of vertical drifts was consistent with that of the ESF occurrence rates for different local time sectors and solar flux conditions. After the key moment of substorms, the ESF occurrence rates fluctuated with epoch time, which was correlated with disturbed vertical drifts. As proposed by many studies (e.g. Stolle et al., 2008; Smith et al., 2016), the enhanced upward drifts maximize the linear growth rate of the Generalized Rayleigh–Taylor instability and contribute to the generation of ESF in two ways. (1) The upward drifts directly contribute to the linear growth rate of the GRT instability; (2) The drifts additionally elevate the F region to a region of lower ion-neutral collision frequencies increasing even further the GRT linear growth rate. On the other hand, the weakened upward drifts, or downward drifts could inhibit the growth of ESF. This scenario was used to explain the high occurrence rate of ESF after sunset. It also explains the high ESF occurrence rates post-midnight during low solar flux (Smith et al., 2016). In addition, both prompt penetration and disturbance dynamo can cause electric field perturbations during substorms. The timing is a critical factor in separating the two sources (Simpson & Bahr, 2020 Xiong et al., 2015). The prompt penetration electric field is derived from the dawn-to-dusk convection electric field and drives upward disturbance drifts at dayside and downward disturbance drifts at nighttime. The effect is almost synchronous with the time scale of about a few hours. In contrast, the disturbance dynamo electric field drives opposite drifts to the prompt

penetration electric field, and it needs more time to affect the equatorial ionosphere (Fejer et al., 2008). In this study, a significant response is observed at around Δt = 0.5 h and Δt = 3.0 h, which could be associated with prompt penetration and disturbance dynamo electric field, respectively.

The superposed epoch analysis results demonstrate that response of the ESF to the equatorial ionosphere to the energy deposited into the high latitude thermosphere is a comprehensive effect of PPEF and DDEF. To further confirm which electric field is primarily responsible for the occurrence of ESF during a substorm, the lag time, or delay between the AE index and ESF should be taken into consideration. As mentioned above, it takes different times for the disturbance driven by PPEF and DDEF to influence the equatorial ionosphere (Fejer et al., 1999). In addition, there may also be a delay in the response of the ESF to the drift, so timing is a critical factor in separating the two sources (Xiong et al., 2015). Hence, we set the parameter dt, which stands for the delay time between ESF observation and the AE index. ESF observation made by JULIA is delayed by dt, then the occurrence rate of ESF is calculated as a function of AE. The relationship between ESF occurrence rate and AE is also investigated. We have tested different values of dt in the range of 0–6 h with a time step of 0.5 h. Figure 5a displays the correlation coefficients between the ESF occurrence rate and the AE index from 0 to 6.0 h of delay time. The correlation coefficients of the 18–00 LT sector are positive from 0 to about 2.5 h under all solar flux conditions, with the highest values occurring in 1, 0.5, and 1 h, which are 0.83, 0.63, and 0.6, respectively. The correlation coefficients turn negative after 2.5 h and fell to the lowest value at 3.5, 3.5, and 4 h, which are −0.61, −0.83, and −0.91, respectively. The variation of correlation coefficients of 00–06 LT is opposite to that of 18–24 LT. Negative correlation coefficients are obtained between 0 and 2 h, while positive correlation coefficients are obtained around 2 h. The minimum values are −0.85, −0.69, and −0.74 at 0, 0.5 and 0 h; while the maximum values are obtained at 3, 3.5, and 3, which are 0.8, 0.82, and 0.94, respectively. From an overall perspective, the greatest absolute values of coefficients are obtained with 3–3.5 h lag for each local time and solar flux condition. Figure 5b displays the ESF occurrence rate in relation to the AE index with 3–3.5 h lag for the different local time and solar flux conditions. There is a noticeable linear relationship between the rate of ESF occurrence and the AE index. In our analysis, the correlation coefficients serve as the criterion for determining the effect of AE on ESF. Lag time dt and corresponding coefficients are presented in the upper left corner of each panel. For post-sunset sector (18–24 LT), delays with the highest correlation coefficients for low, moderate, and high solar flux conditions are 3.5, 3.0, and 3.0 h, respectively. The result exhibits that the ESF occurrence rate and AE index are correlated negatively in the 18–24 LT sector. For the post-midnight sector (00–06 LT), the maximum correlation coefficients during all solar flux conditions appear at dt = 3.0 h, 3.5 h and 3.0 h, respectively. The corresponding correlation coefficients are 0.805, 0.819, and 0.94, respectively, showing a strong positive linear correlation, which is opposite to the correlations of the post-sunset sector. It can be seen from Figure 5 that the maximum value of correlation corresponds to a lag time of 3–3.5 h, revealing that the DDEF may play a more important role than PPEF.

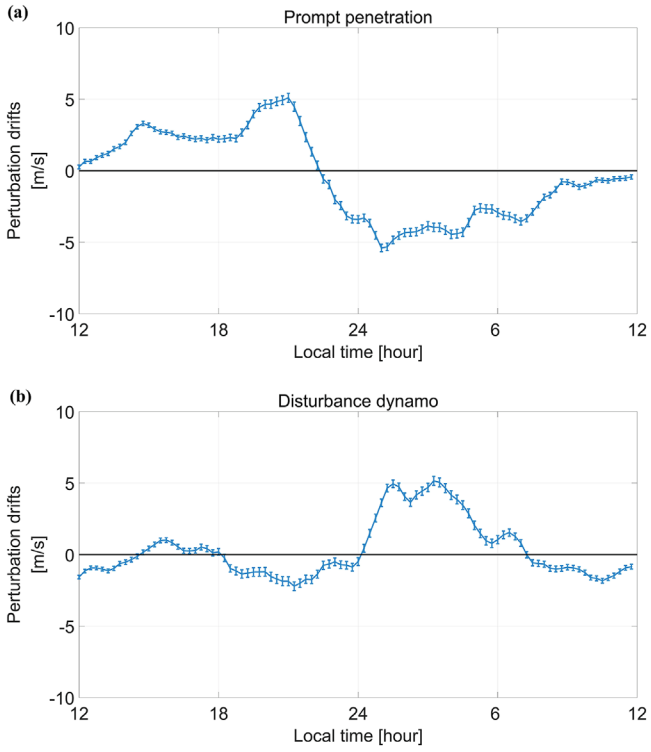

Figure 6. Averaged equatorial disturbance vertical plasma drifts (positive upward) as a step function of local time.

4.2 The local time dependence of ESF response to substorms

The results of Figures 3–5 reveal notable local time dependence for the substorm effect on ESF. More specifically, approximately 1 h after the substorm, the ESF occurrence rate increased for a post-sunset sector (18–24 LT) but decreased for a post-midnight sector (00–06 LT); while about 3 h after the substorm, post-sunset ESF was suppressed and the post-midnight ESF was promoted. Similar local dependence characteristics for drifts were obtained under different solar flux conditions, indicating that disturbance drifts played an important role in the local time dependence of ESF. Therefore, we investigated the local-time variation of the disturbance drifts caused by PPEF and DDEF during substorms, respectively.

In this study, the PPEF perturbation drifts were obtained by averaging the perturbation drifts over 0–1 h after the onset of substorm determined by the AL-based algorithm (see Sector 2), while DDEF perturbation drifts were obtained by averaging the perturbation drifts over 3–4 h after substorms onset. Figure 6a depicts the local time variation of perturbation drifts caused by prompt penetration electric fields, which agrees well with averaged values derived from Jicamarca radar observations (Fejer et al., 1999; Huang, 2009) and results from global convection models (Fejer et al., 2008). It showed large upward drifts near sunrise, followed by a reversion around 2100 LT, and then a downward perturbation drifts that lasted until 0600 LT. The result also verifies the perturbation electric field pattern associated with storm-time changes (Navarro et al., 2019). Figure 6b presents the result of perturbation drifts driven by

the disturbance dynamo electric field. It shows small downward disturbance drifts between 18 and 24 LT and larger upward post-midnight drifts until 07 LT. The greatest nighttime upward drifts occur around 0300 LT, with a maximum value of 6 m/s. The local time variation of the drifts driven by the disturbance dynamo electric field is anti-correlated with that of the prompt penetration, which explains well the local time dependence of ESF occurrence in this study. Specifically, the behaviour of ESF occurrence rate and vertical drifts exhibits increasing for 18–24 LT and decreasing for 00–06 LT around the key time ($\Delta t = 0$), which is thought to be the effect of prompt penetration electric field. At around $\Delta t = 3$ h, the post-sunset ESF is suppressed while the midnight and post-midnight ESF is promoted, which is attributed to the effect of disturbance dynamo electric field.

5 Summary and conclusions

The comprehensive analysis results of almost 18 years (2000–2017) of measurements made by the Jicamarca Radio Observatory incoherent scatter radar (ISR) and coherent backscatter radar (JULIA) were employed to investigate the response of the ESF to substorms. In this study, our work focused on the effect of non-storm time substorms on equatorial ionospheric irregularities and provides new insights based on extensive measurements. First, a post-midnight ESF event at 0300 LT on October 1, 2008, was presented. The upward disturbance drift, which was deemed to be associated with a sole substorm, led to the generation and growth of the ESF. Then, we checked the AE index variation as a function of local time for ESF and non-ESF epochs. The response of ESF occurrence rate and disturbance drifts to substorm is investigated using superposed epoch analysis for two local time sectors (post-sunset: 18–24 LT and post-midnight: 00–06 LT) and three ranges of solar flux conditions (low: P107 < 90, moderate: 90 < P107 < 120, and high: P107 > 120 SFU). the results showed obvious local time dependence. The main findings of our investigation are summarized below:

1. There is a strong correlation between the occurrence of ESF and substorms, and the impacts of a substorm might last for more than 12 h. In the meantime, the perturbation vertical drift follows the same pattern as the ESF occurrence rate;
2. the response of equatorial spread F to substorm shows local time dependence: For the post-sunset (1800–2400 LT) sector, the occurrence rate of equatorial spread F increased to a maximum at about 0.5 h and decreased to a minimum value around 3.0 h after the substorm; while for post-midnight (0000–0600 LT) sector the occurrence rate showed an opposite response. The local time dependence is due to the opposite perturbation drift caused by PPEF and DDEF;
3. the correlation coefficient between the AE index and the occurrence rate of ESF is greatest when the lag time is 3–3.5 h. This is when the disturbance dynamo process becomes dominant in equatorial ionospheric dynamics, implying that the effect of disturbance dynamo electric fields may be more substantial than that of prompt penetration electric fields during a substorm.

Acknowledgements. We thank the Space Physics Data Facility at Goddard Space Flight Center (https://omniweb.gsfc.nasa.gov/) for providing the solar wind, IMF and geomagnetic activity data. We also thank the Jicamarca Radio Observatory for providing ISR drift and JULIA data. The radar measurements used in this study can be obtained from the Madrigal database (http://jro.igp.gob.pe/madrigal/). The work was supported by the National Natural Science Foundation of China through grant 42074185. Chao Xiong is partly supported by the ISSI projects "Resolving the Generation Mechanisms and Electrodynamical Effects of Medium Scale Traveling Ionospheric Disturbances (MSTIDs)" and "Multi-Scale Magnetosphere-Ionosphere-Thermosphere Interaction". The editor thanks S. Tulasi Ram and an anonymous reviewer for their assistance in evaluating this paper.

References

Aa E, Zou S, Ridley A, Zhang S, Coster AJ, Erickson PJ, Ren J. 2019. Merging of storm time midlatitude traveling ionospheric disturbances and equatorial plasma bubbles. *Space Weather* **17(2)**: 285–298. https://doi.org/10.1029/2018SW002101.

Aarons J. 1993. The longitudinal morphology of equatorial F-layer irregularities relevant to their occurrence. *Space Sci Rev* **63(3)**: 209–243. https://doi.org/10.1007/BF00750769.

Abdu MA, Bittencourt JA, Batista IS. 1981. Magnetic declination control of the equatorial F region dynamo electric field development and spread F. *J Geophys Res Space Phys* **86(A13)**: 11443–11446. https://doi.org/10.1029/JA086iA13p11443.

Abdu MA, Batista IS, Takahashi H, MacDougall J, Sobral JH, Medeiros AF, Trivedi NB. 2003. Magnetospheric disturbance induced equatorial plasma bubble development and dynamics: A case study in Brazilian sector. *J Geophys Res Space Phys* **108 (A12)**: 1449. https://doi.org/10.1029/2002JA009721.

Basu B. 2002. On the linear theory of equatorial plasma instability: Comparison of different descriptions. *J Geophys Res Space Phys* **107(A8)**: SIA-18. https://doi.org/10.1029/2001JA000317.

Blanc M, Richmond AD. 1980. The ionospheric disturbance dynamo. *J Geophys Res Space Phys* **85(A4)**: 1669–1686. https://doi.org/10.1029/JA085iA04p01669.

Borovsky JE, Shprits YY. 2017. Is the Dst index sufficient to define all geospace storms? *J Geophys Res Lett* **122(11)**: 11–543. https://doi.org/10.1002/2017JA024679.

Burke WJ, de La Beaujardière O, Gentile LC, Hunton DE, Pfaff RF, Roddy PA, Wilson GR. 2009. C/NOFS observations of plasma density and electric field irregularities at post-midnight local times. *Geophys Res Lett* **36(18)**. https://doi.org/10.1029/2009GL038879.

Cherniak I, Zakharenkova I. 2022. Development of the storm-induced ionospheric irregularities at equatorial and middle latitudes during the 25–26 August 2018 geomagnetic storm. *Space Weather* **20(2)**: e2021SW002891. https://doi.org/10.1029/2021SW002891.

Conker RS, El-Arini MB, Hegarty CJ, Hsiao T. 2003. Modeling the effects of ionospheric scintillation on GPS/satellite-based augmentation system availability. *Radio Sci* **38(1)**: 1-1–1-23. https://doi.org/10.1029/2000RS002604.

Doherty P, Coster AJ, Murtagh W. 2004. Space weather effects of October–November 2003. *GPS Solut* **8(4)**: 267–271. https://doi.org/10.1007/s10291-004-0109-3.

Fejer BG, Scherliess L, De Paula ER. 1999. Effects of the vertical plasma drift velocity on the generation and evolution of equatorial spread F. *J Geophys Res Space Phys* **104(A9)**: 19859–19869. https://doi.org/10.1029/1999JA900271.

Fejer BG, Jensen JW, Su SY. 2008. Seasonal and longitudinal dependence of equatorial disturbance vertical plasma drifts. *Geophys Res Lett* **35(20)**. https://doi.org/10.1029/2008GL035584.

Fejer BG. 2011. Low latitude ionospheric electrodynamics. *Space Sci Rev* **158(1)**: 145–166. https://doi.org/10.1007/s11214-010-9690-7.

Fejer BG, Navarro LA, Sazykin S, Newheart A, Milla MA, Condor P. 2021. Prompt penetration and substorm effects over Jicamarca during the September 2017 geomagnetic storm. *J Geophys Res Space Phys* **126(8)**: e2021JA029651. https://doi.org/10.1029/2021JA029651.

Hashimoto KK, Kikuchi T, Tomizawa I, Nagatsuma T. 2017. Substorm overshielding electric field at low latitude on the nightside as observed by the HF Doppler sounder and magnetometers. *J Geophys Res Space Phys* **122(10)**: 10–851. https://doi.org/10.1002/2017JA024329.

Hlubek N, Berdermann J, Wilken V, Gewies S, Jakowski N, Wassaie M, Damtie B. 2014. Scintillations of the GPS, GLONASS, and Galileo signals at equatorial latitude. *J Space Weather Space Clim* **4**: A22. https://doi.org/10.1051/swsc/2014020.

Huang CS. 2009. Eastward electric field enhancement and geomagnetic positive bay in the dayside low-latitude ionosphere caused by magnetospheric substorms during sawtooth events. *Geophys Res Lett* **36(18)**. https://doi.org/10.1029/2009GL040287.

Huang CS. 2012. Statistical analysis of dayside equatorial ionospheric electric fields and electrojet currents produced by magnetospheric substorms during sawtooth events. *J Geophys Res Space Phys* **117(A2)**. https://doi.org/10.1029/2011JA017398.

Huang CS, Hairston MR. 2015. The postsunset vertical plasma drift and its effects on the generation of equatorial plasma bubbles observed by the C/NOFS satellite. *J Geophys Res Space Phys* **120(3)**: 2263–2275. https://doi.org/10.1002/2014JA020735.

Hui D, Chakrabarty D, Sekar R, Reeves GD, Yoshikawa A, Shiokawa K. 2017. Contribution of storm time substorms to the prompt electric field disturbances in the equatorial ionosphere. *J Geophys Res Space Phys* **122(5)**: 5568–5578. https://doi.org/10.1002/2016JA023754.

Hysell DL, Burcham JD. 2002. Long term studies of equatorial spread F using the JULIA radar at Jicamarca. *J Atmos Terr Phys* **64(12–14)**: 1531–1543. https://doi.org/10.1016/S1364-6826(02)00091-3.

Kamide Y, Baumjohann W, Daglis IA, et al. 1998. Current understanding of magnetic storms: Storm-substorm relationships. *J Geophys Res Space Phys* **103(A8)**: 17705–17728. https://doi.org/10.1029/98JA01426.

Kelley MC, Haerendel G, Kappler H, Valenzuela A, Balsley BB, Carter DA, Ecklund WL, Carlson CW, Häusler B, Torbert R. 1976. Evidence for a Rayleigh–Taylor type instability and upwelling of depleted density regions during equatorial spread F. *Geophys Res Lett* **3(8)**: 448–450. https://doi.org/10.1029/GL003i008p00448.

Kelley MC, Larsen MF, La Hoz C, McClure JP. 1981. Gravity wave initiation of equatorial spread F: A case study. *J Geophys Res: Space Phys* **86**: 9087. https://doi.org/10.1029/JA086iA11p09087.

Kikuchi T, Lühr H, Schlegel K, Tachihara H, Shinohara M, Kitamura T-I. 2000. Penetration of auroral electric fields to the equator during a substorm. *J Geophys Res: Space Phys* **105(A10)**: 23251–23261. https://doi.org/10.1029/2000JA900016.

Kikuchi T, Hashimoto KK, Nozaki K. 2008. Penetration of magnetospheric electric fields to the equator during a geomagnetic storm. *J Geophys Res Space Phys* **113(A6)**. https://doi.org/10.1029/2007JA012628.

Li G, Ning B, Abdu MA, Yue X, Liu L, Wan W, Hu L. 2011. On the occurrence of postmidnight equatorial F region irregularities during the June solstice. *J Geophys Res: Space Phys* **116(A4)**. https://doi.org/10.1029/2010ja016056.

Li G, Ning B, Wang C, Abdu MA, Otsuka Y, Yamamoto M, Chen J. 2018. Storm-enhanced development of postsunset equatorial plasma bubbles around the meridian 120 E/60 W on 7–8 September 2017. *J Geophys Res Space Phys* **123**: 7985–7998. https://doi.org/10.1029/2018JA025871.

McClure JP, Hanson Hoffman J H. 1977. Plasma bubbles and irregularities in the equatorial ionosphere. *J Geophys Res Space Phys* **82(19)**: 2650–2656. https://doi.org/10.1029/JA082i019p02650.

Navarro LA, Fejer BG, Scherliess L. 2019. Equatorial disturbance dynamo vertical plasma drifts over Jicamarca: Bimonthly and solar cycle dependence. *J Geophys Res Space Phys* **124(6)**: 4833–4841. https://doi.org/10.1029/2019JA026729.

Newell PT, Gjerloev JW. 2011. Evaluation of SuperMAG auroral electrojet indices as indicators of substorms and auroral power. *J Geophys Res Space Phys* **116(A12)**. https://doi.org/10.1029/2011JA016779.

Nicolls MJ, Kelley MC, Vlasov MN, Sahai Y, Chau JL, Hysell DL, Lima WLC. 2006. Observations and modeling of post-midnight uplifts near the magnetic equator. *Ann Geophys* **24**: 1317–1331. https://doi.org/10.5194/angeo-24-1317-2006.

Paul KS, Haralambous H, Oikonomou C, Paul A, Belehaki A, Ioanna T. 2018. Multi-station investigation of spread F over Europe during low to high solar activity. *J Space Weather Space Clim* **8**: A27. https://doi.org/10.1051/swsc/2018006.

Rentz S, Lühr H. 2008. Climatology of the cusp-related thermospheric mass density anomaly, as derived from CHAMP observations. *Ann Geophys* **26(9)**: 2807–2823. https://doi.org/10.5194/angeo-26-2807-2008.

Rout D, Pandey K, Chakrabarty D, Sekar R, Lu X. 2019. Significant electric field perturbations in low latitude ionosphere due to the passage of two consecutive ICMEs during 6–8 September 2017. *J Geophys Res Space Phys* **124(11)**: 9494–9510. https://doi.org/10.1029/2019JA027133.

Simpson F, Bahr K. 2020. Estimating the electric field response to the Halloween 2003 and September 2017 magnetic storms across Scotland using observed geomagnetic fields, magnetotelluric impedances and perturbation tensors. *J Space Weather Space Clim* **10**: 48. https://doi.org/10.1051/swsc/2020049.

Singh S, Johnson FS, Power RA. 1997. Gravity wave seeding of equatorial plasma bubbles. *J Geophys Res Space Phys* **102**: 7399–7410. https://doi.org/10.1029/96JA03998.

Singh R, Sripathi S. 2020. A statistical study on the local time dependence of equatorial spread F (ESF) irregularities and their relation to low-latitude Es layers under geomagnetic storms. *J Geophys Res Space Phys* **125(1)**: e2019JA027212. https://doi.org/10.1029/2019JA027212.

Smith JM, Rodrigues FS, Fejer BG, Milla MA. 2016. Coherent and incoherent scatter radar study of the climatology and day-to-day variability of mean F region vertical drifts and equatorial spread F. *J Geophys Res Space Phys* **121(2)**. https://doi.org/10.1002/2015JA021934.

Stolle C, Luehr H, Fejer BG. 2008. Relation between the occurrence rate of ESF and the equatorial vertical plasma drift velocity at sunset derived from global observations. *Ann Geophys* **26(12)**. https://doi.org/10.5194/angeo-26-3979-2008.

Sultan PJ. 1996. Linear theory and modeling of the Rayleigh–Taylor instability leading to the occurrence of equatorial spread F. *J Geophys Res Space Phys* **101(A12)**: 26875–26891. https://doi.org/10.1029/96JA00682.

Sunda S, Sridharan R, Vyas BM, Khekale PV, Parikh KS, Ganeshan AS. 2015. Satellite-based augmentation systems: A novel and cost-effective tool for ionospheric and space weather studies. *Space Weather* **13(1)**: 6–15. https://doi.org/10.1002/2014SW001103.

Thampi SV, Yamamoto M, Tsunoda RT, Otsuka Y, Tsugawa T, Uemoto J. 2009. First observations of large-scale wave structure and equatorial spread F using CERTO radio beacon on the C/NOFS satellite. *Geophys Res Lett* **36**. https://doi.org/10.1029/2009GL039887.

Wan X, Xiong C, Rodriguez-Zuluaga J, Kervalishvili GN, Stolle C, Wang H. 2018. Climatology of the occurrence rate and amplitudes of local time distinguished equatorial plasma depletions observed by Swarm satellite. *J Geophys Res Space Phys* **123**: 3014–3026. https://doi.org/10.1002/2017JA025072.

Wan X, Xiong C, Wang H, Zhang K, Zheng Z, He Y, Yu L. 2019. A statistical study on the climatology of the Equatorial Plasma Depletions occurrence at topside ionosphere during geomagnetic disturbed periods. *J Geophys Res Space Phys* **124**. https://doi.org/10.1029/2019JA026926.

Watanabe S, Oya H. 2010. Occurrence characteristics of low latitude ionosphere irregularities observed by impedance probe on board the hinotori satellite. *Earth Planets Space* **38(2)**: 125–149. https://doi.org/10.5636/jgg.38.125.

Xiong C, Park J, Luehr H, Stolle C, Ma SY. 2010. Comparing plasma bubble occurrence rates at champ and grace altitudes during high and low solar activity. *Ann Geophys* **28(9)**: 1647–1658. https://doi.org/10.5194/angeo-28-1647-2010.

Xiong C, Lühr H, Fejer BG. 2015. Global features of the disturbance winds during storm time deduced from CHAMP observations. *J Geophys Res Space Phys* **120(6)**: 5137–5150. https://doi.org/10.1002/2015JA021302.

Xiong C, Stolle C, Lühr H. 2016a. The swarm satellite loss of GPS signal and its relation to ionospheric plasma irregularities. *Space Weather* **14(8)**: 563–577. https://doi.org/10.1002/2016SW001439.

Xiong C, Lühr H, Fejer BG. 2016b. The response of equatorial electrojet, vertical plasma drift, and thermospheric zonal wind to enhanced solar wind input. *J Geophys Res Space Phys* **6**: 5653–5663. https://doi.org/10.1002/2015JA022133.

Zhan W, Rodrigues FS, Milla MA. 2018a. On the genesis of post-midnight equatorial spread F: Results for the American/Peruvian sector. *Geophys Res Lett* **45(15)**: 7354–7361. https://doi.org/10.1029/2018GL078822.

Zhan W, Rodrigues FS. 2018b. June solstice equatorial spread F in the American sector: A numerical assessment of linear stability aided by incoherent scatter radar measurements. *J Geophys Res: Space Phys* **123(1)**: 755–767. https://doi.org/10.1002/2017JA024969.

Zhang K, Wang H, Liu J, Zheng Z, He Y, Gao J, Zhong Y. 2021a. Dynamics of the tongue of ionizations during the geomagnetic storm on September 7, 2015. *J Geophys Res Space Phys* **126(6)**: e2020JA029038. https://doi.org/10.1029/2020JA029038.

Zhang K, Wang H, Liu J, Zheng Z, He Y, Gao J, Zhong Y. 2021b. Effects of subauroral polarization streams on the equatorial electrojet during the geomagnetic storm on June 1, 2013. *J Geophys Res Space Phys* **126(10)**: e2021JA029681. https://doi.org/10.1029/2021JA029681.

Zhang K, Wang H, Wang W. 2022. Local time variations of the equatorial electrojet in simultaneous response to subauroral polarization streams during quiet time. *Geophys Res Lett* **49(7)**: e2022GL098623. https://doi.org/10.1029/2022GL098623.

Cite this article as: Gao S, Cai H, Zhan W, Wan X, Xiong C, et al. 2023. Characterization of local time dependence of equatorial spread F responses to substorms in the American sector. *J. Space Weather Space Clim.* **13**, 2. https://doi.org/10.1051/swsc/2022039.